Anomalous Detachment Behavior and Directional Reconstruction Regulation of Leaching-Type Precatalysts for Industrial Water Electrolyzers

Xiong Liu, Ruiting Guo, Minghao Guo, Kun Ni, Meng Huang, Jiashen Meng, Xiaohong Xie, Dongyuan Zhao, Liqiang Mai,* and Chaojiang Niu**

Current reconstruction chemistry studies are mainly operated at the laboratory scale, where the operating parameters are different from those used in industrial water electrolyzers. This gap leads to unclear reconstruction behaviors under industrial conditions and constrains the application of catalysts. Here, this work presents a new reconstruction mechanism and anomalous detachment phenomena observed in leaching-type oxygen-evolving precatalysts under industrial conditions, different from the reported results obtained under laboratory conditions. The identified detachment issues are closely linked to the production of a potassium salt separate phase, which proves sensitive to the local environment, and its instability easily leads to catalyst stripping from the substrate. By establishing detachment critical point and operating parameter-detachment correlation, a targeted reconstruction strategy is proposed to achieve smooth ligand leaching and effectively solve the detachment issue. Theoretical analyses validate the dual-site regulation in directionally reconstructed catalysts with optimized intermediate adsorption. Under industrial conditions, the coupled electrolyzer delivers an industrial-level current density at low cell voltage with prolonged durability, 1 A cm^{-2} at 2 V for over 340 h. This work bridges the gap of leaching-type precatalysts between laboratory test conditions and industrial operating conditions.

1. Introduction

Surface reconstruction widely exists in metal-based catalytic materials during oxygen evolution catalysis, endowing distinct physical and chemical properties in the reconstructed material compared to their precatalysts.[1–3] These derived reconstructed materials cannot be directly synthesized by using traditional methods due to their variable structures such as 3D multilevel porous structure, sub-10 nm nanoparticle interconnecting structure, low crystallinity, and abundant vacancy. Several strategies have been explored to regulate the sur-/interface structures of the reconstructed catalysts such as precatalyst composition[4,5] and size[6] design, electrolyte mediation (concentration and ion type),[7,8] external field effect (temperature and atmosphere),[9,10] and heterogeneous reaction treatment.[11] Although significant progress has been made in understanding the influencing

---

X. Liu, C. Niu
School of Materials Science and Engineering
Zhengzhou University
Zhengzhou 450001, P. R. China
E-mail: niuchaojiang@zzu.edu.cn
R. Guo, J. Meng, L. Mai
State Key Laboratory of Advanced Technology for Materials Synthesis and Processing
Wuhan University of Technology
Wuhan 430070, P. R. China
E-mail: mlq518@whut.edu.cn
M. Guo, K. Ni
CAS Key Laboratory of Materials for Energy Conversion
Department of Materials Science and Engineering
University of Science and Technology of China
Anhui 230026, P. R. China
E-mail: nikun@ustc.edu.cn

M. Huang
Sanya Science and Education Innovation Park
Wuhan University of Technology
Sanya 572000, P. R. China
X. Xie
School of Chemistry and Chemical Engineering
Chongqing University
Chongqing 401331, P. R. China
D. Zhao
Laboratory of Advanced Materials
Shanghai Key Laboratory of Molecular Catalysis and Innovative Materials
State Key Laboratory of Molecular Engineering of Polymers
School of Chemistry and Materials
Fudan University
Shanghai 200433, P. R. China

The ORCID identification number(s) for the author(s) of this article can be found under https://doi.org/10.1002/adma.202313931

DOI: 10.1002/adma.202313931

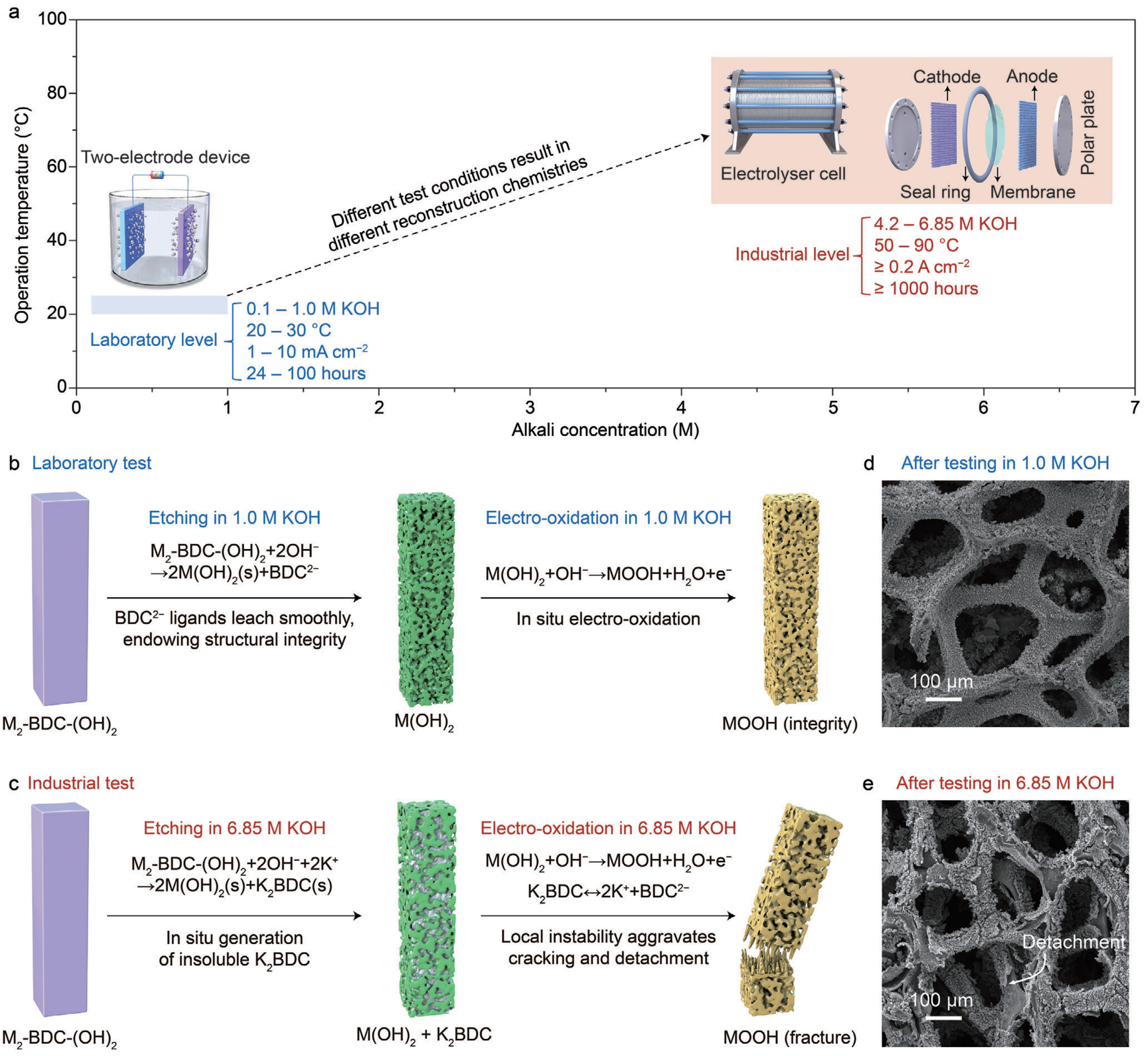

Figure 1. a) Comparative plot of the two key evaluation parameters (i.e., alkali concentration and operation temperature) used in the study of HER/OER catalysts and their coupled alkaline water electrolysis devices between laboratory test conditions and industrial operating conditions. b, c) Schematic diagram of the reconstruction process of M_2-BDC-$(OH)_2$ precatalysts undergoing OER in laboratory test conditions of 1 м KOH (b) and industrial operating condition of 6.85 м KOH (c), which displays different reconstruction chemistry and mechanical stability of the reconstructed catalysts. These differences depend on whether there is a formation of insoluble K_2BDC. d, e) SEM images of $Ni_{0.5}Fe_{0.5}$-BDC/NF samples after testing in 1 м KOH (d) and 6.85 м KOH (e), respectively.

factors and regulating reconstruction behavior,[12–16] the intrinsic reconstruction mechanism and targeted reconstruction engineering still remain great challenges.

Furthermore, the current reconstruction chemistry studies and performance assessments remain confined to the laboratory level, in which the operating parameters are far from realistic industrial ones.[1] Specifically, in industrial alkaline water electrolysis, the electrolyzer generally necessitates hydrogen production at notably high current densities reaching amperes per square centimeter (A cm^{-2}) level, involves high potassium hydroxide (KOH) concentrations ranging from 20 to 30 wt% (equivalent to 4.2–6.85 м), high temperatures within the range of 50 to 90 °C, and sustained operation exceeding 1000 h.[17,18] In contrast, traditional laboratory studies on hydrogen/oxygen evolution reaction (HER/OER) catalysts and their coupled devices predominantly focus on low current densities (1–10 mA cm^{-2}), low KOH concentrations (0.1–1 м), room temperature conditions (20–30 °C), and abbreviated operating durations (24–100 h), as shown in **Figure** 1a. This gap will bring different reconstruction chemistries and various application problems.

The reconstruction degree, configuration, mechanical stability, and electrochemical performance of reconstructed catalysts are profoundly impacted by various operating conditions including applied bias/current, test temperature, solution type, and solution concentration. First, different biases induce distinct surface chemical modifications in the catalyst, and the surface structure determines the catalytic mechanisms.[19] When the bias exceeds the redox potential of elements, it leads to surface instability and alterations in valence states. Second, the industrial-level current density (A cm^{-2}) implies swift gas spillover and diffusion, necessitating robust mechanical stability in the reconstructed catalyst.[20] Poor mechanical stability isolates the active component or strips the catalyst into the solution. Furthermore, current density influences the adsorption free energy levels of intermediates at various coverages, leading to different catalytic performance trends between industrially relevant and laboratory-scale current densities.[21] Third, the reconstruction degrees of certain precatalysts exhibit a strong correlation with temperature, exemplified by molybdates,[9] resulting in totally different catalyst configurations and catalytic performances. Fourth, the reconstruction behaviors of precatalysts are influenced by the presence of specific anions in the solution such as erythrites.[8] These typical examples prompt two critical questions: what are the reconstruction chemistries of precatalysts under realistic industrial operating conditions? How to obtain high-performance reconstructed catalysts for practical applications?

To address the above two questions and bridge the gap between laboratory test conditions and industrial operating conditions, we use a terephthalic acid-coordinated metal-based oxygen evolution precatalyst to identify and address crucial mechanical stability problems in industrial alkaline water electrolysis applications. Our study elucidates the differences in reconstruction chemistries (Figure 1b,c) and mechanical stability (Figure 1d,e) arising from variations in alkali concentration between laboratory test conditions and industrial operating conditions. The underlying causes and influencing factors leading to the detachment of the reconstructed catalyst from the nickel foam substrate are systematically disclosed. Additionally, the critical point of detachment and operating parameter-detachment correlation are established. Ultimately, a directional reconstruction regulation through a gradient test strategy is proposed to effectively solve this issue under realistic industrial conditions.

2. Results and Discussion

Terephthalic acid-coordinated NiFe-based precatalyst loaded on the 3D conductive nickel foam skeleton (denoted as $Ni_{1-x}Fe_x$-BDC/NF, $x = 0$–0.9) has been synthesized utilizing a facile wet-chemical approach. This synthesis includes heterogeneous nucleation growth among bivalent nickel ions, bivalent iron ions, and terephthalic acid ligands in an aqueous solution. Illustratively, considering $Ni_{0.5}Fe_{0.5}$-BDC/NF as a representative case, the color transformation of the entire nickel foam from silver to dark red is observed after the synthetic reaction (Figure S1a, Supporting Information). The mass loading of $Ni_{0.5}Fe_{0.5}$-BDC reaches ≈10 mg cm^{-2}, which is beneficial for improving the geometric activity of the realistic catalyst. Importantly, the presented synthesis method exhibits scalability, allowing for large-scale production with an impressive yield of ≈528 cm^2 in one pot when using a larger reaction vessel (Figure S1b, Supporting Information). The micron-scale bulk $Ni_{0.5}Fe_{0.5}$-BDC grows uniformly on the entire foam skeleton, with its chemical composition confirmed as NiFe-BDC-$(OH)_2$ via electron microscopy and spectral analyses (Figure S1c–f, Supporting Information). Additionally, by manipulating the Ni/Fe ratios in the raw materials, diverse $Ni_{1-x}Fe_x$-BDC products with variable ratios are successfully obtained (Figure S2, Supporting Information). It is noteworthy that the effective incorporation of iron into Ni-BDC is hindered when using ferric iron sources. These samples are all dark green, which is similar to that of pure Ni-BDC (Figure S3, Supporting Information).

2.1. The Reconstruction and Detachment Phenomena Under Industrial Conditions

First, in situ electrochemistry-Raman spectroscopy tests were conducted to identify phase reconstruction and the real active species of $Ni_{0.5}Fe_{0.5}$-BDC/NF under different operating conditions. The $Ni_{0.5}Fe_{0.5}$-BDC/NF was operated at a constant current of 1 mA through chronopotentiometric tests in two distinct KOH concentrations, namely 1 and 6.85 м. The accompanying time-dependent Raman spectra were simultaneously recorded (Figure S4, Supporting Information). In both cases, the characteristic Raman peaks associated with $Ni_{0.5}Fe_{0.5}$-BDC (866, 1143, 1429, and 1617 cm^{-1}) exhibit complete disappearance, and new peaks (485 and 557 cm^{-1}) which belong to the bending and stretching vibrations of nickel (oxy)hydroxide emerge after testing. This indicates that the active phases in different alkali concentrations are consistently (oxy)hydroxides. Notably, the broad peak centered at 485 cm^{-1} exhibits a more positive location compared to the characteristic peak of pure nickel (oxy)hydroxide at 475 cm^{-1}. This shift is attributed to the presence of reconstructed species with incorporated Fe.[22] When testing in 6.85 м KOH, the duration for the disappearance of $Ni_{0.5}Fe_{0.5}$-BDC and the appearance of the (oxy)hydroxide phase is observed to be shorter than that in 1 м KOH. This observation suggests a more rapid reconstruction behavior in high-concentration alkali environments.

Figure 2a presents real-time monitoring photos of $Ni_{0.5}Fe_{0.5}$-BDC/NF precatalyst electrodes subjected to a constant current density for OER in two distinct KOH concentrations, namely 6.85 (top) and 1 м (bottom). The observed results reveal distinct behavior in response to varying alkaline conditions. Specifically, in an industrial high-concentration alkali environment, there is a consistent phenomenon of material detachment from the electrodes, subsequently depositing at the solution's base. Conversely, such detachment is not observed in the low-concentration alkali environment (1 м KOH). Notably, the severity of the detachment issue is exacerbated under high oxygen evolution current densities (Figure 2b). This phenomenon confirms the poor mechanical stability of the reconstructed catalyst, particularly in more demanding operating parameters.

The phenomenon of detachment has been observed in various states (Figure 2c) including the static state, HER, and the urea oxidation reaction (UOR). Upon immersion in 6.85 м KOH, the generation of loosely bound species occurs, which easily fall off the foam skeleton. The stripped irregular solids are confirmed as the hydroxide phase (Figure S5, Supporting Information), which originate from the fracture of the catalyst growing on the

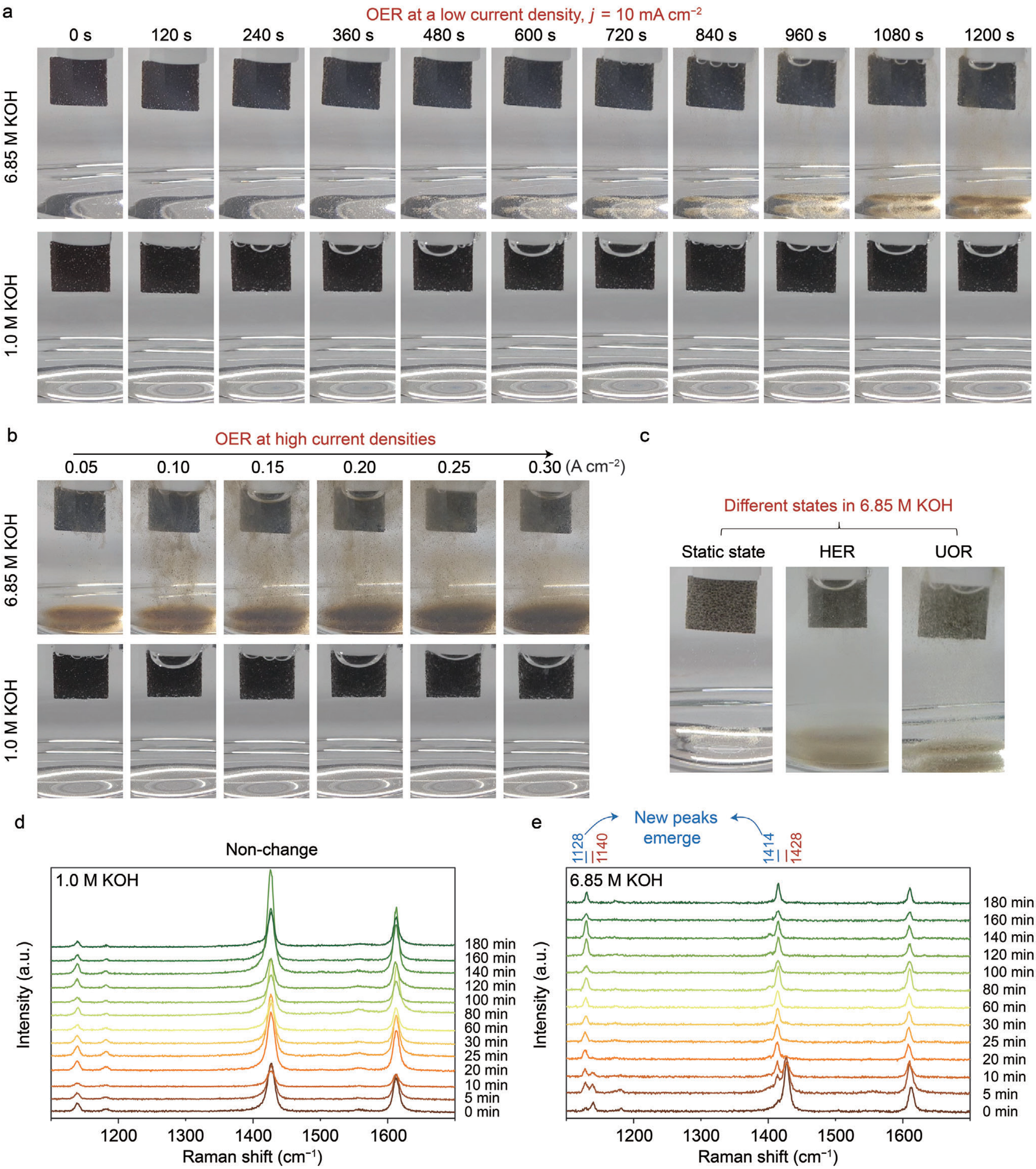

Figure 2. a) Real-time monitoring photos of catalyst electrodes (size: 10 mm × 10 mm) in 1 M KOH (bottom) and 6.85 M KOH (top) at a constant low current density of $j = 10$ mA cm^{-2}. b) Real-time monitoring photos of catalyst electrodes in 1 M KOH (bottom) and 6.85 M KOH (top) at different current densities. c) Optical photos of catalyst electrodes after static state, HER, and UOR tests in 6.85 M KOH. d,e) In situ Raman spectra when immersed in 1 M KOH (d) and 6.85 M KOH (e).

skeleton. The detachment process exhibits variations in speed and severity under different conditions (Figure S6, Supporting Information). Notably, in the static state, the speed and severity of detachment are significantly reduced. This reduction is advantageous as it facilitates a more precise characterization of the detachment processes. Therefore, the origin of catalyst detachment during immersion is emphatically discussed.

Here, the elucidation of the detachment mechanism in immersion experiments holds significance for understanding the electrochemical results. As explained below, insoluble potassium salts, functioning as intermediate products, play a pivotal role in catalytic detachment. However, their instability, stemming from variations in the local environment during electrooxidation, presents challenges in promptly and accurately capturing them in in situ electrochemical experiments. Notably, the catalyst in immersion experiments lacks the electrooxidation and gas spillover steps compared to the electrochemical experiment (Figure 1b,c). This absence implies that intermediates can be stabilized, slowing down catalyst detachment in the immersion experiment and facilitating the detection of intermediates. As shown in Figure 2d,e, the in situ chemistry-Raman spectroscopy results are analyzed when the $Ni_{0.5}Fe_{0.5}$-BDC/NF samples are immersed in 1 м KOH or 6.85 м KOH at different times. Following a 3-h immersion in 1 м KOH, no discernible changes in the Raman peaks are observed. Conversely, immersion in 6.85 м KOH for just 5 min prompts the emergence of new Raman peaks centered at 1128 and 1414 cm^{-1}; the original Raman peaks centered at 1140 and 1428 cm^{-1} completely disappear after 20 min. Despite differences in reconstruction rates and products between in situ electrochemical-Raman and in situ chemical-Raman tests, both processes exhibit etching reactions and detachment phenomena. Furthermore, the emergence of new Raman peaks in Figure 2e coincides with the catalyst detachment time, indicating that these newly identified Raman peaks are crucial for comprehending the detachment mechanism in both chemical and electrochemical processes.

2.2. The Detachment Mechanism

To elucidate the specific species, we conducted a comparative analysis of Raman spectra involving commercial H_2BDC powder, excess H_2BDC-1 м KOH (where excess H_2BDC powder is introduced to 1 м KOH), and H_2BDC-6.85 м KOH mixture (**Figure 3**a). The Raman results for the H_2BDC-6.85 м KOH mixture align with our expectations, indicating that BDC ligands form insoluble salts upon reacting with potassium ions in a high-concentration alkali. Subsequently, varying quantities of white H_2BDC powder were added to 1 mL of both 1 м KOH and 6.85 м KOH solutions and fully dissolved (Figure 3b). A white suspension only becomes evident when 100 mg of H_2BDC is introduced to 1 м KOH, which is attributed to the incomplete dissolution of H_2BDC (Figure 3c). In contrast, a white suspension forms with just 5 mg of H_2BDC in 6.85 м KOH, which results from the production of insoluble K_2BDC. Additionally, by combining 200 µL of the mixture (5 mg H_2BDC + 1 mL of 6.85 м KOH) with an equal volume of deionized water, the resulting solution becomes colorless and transparent (FigureS7, Supporting Information). These results affirm the facile formation of K_2BDC in a high-concentration alkali, with its solubility proving sensitive to solution concentration.

To elucidate the occurrence of the K_2BDC phase during the reaction conducted directly in 6.85 м KOH, we promptly extracted the $Ni_{0.5}Fe_{0.5}$-BDC/NF from the reaction and subjected it to a swift ethanol wash to remove the aqueous solution, thereby preserving the original structure. This approach is chosen due to the exceptionally high solubility and instability of K_2BDC in aqueous solutions, contrasting with its low solubility in ethanol. Then the catalyst, following a reaction in 6.85 м KOH, was conducted by electron microscopy and X-ray diffraction (XRD) characterizations (Figure S8, Supporting Information). The K element exhibits a predominant distribution within the reaction region of the catalyst (left side of the black dashed line). Observation of the reaction zone discloses the presence of fractured areas and two distinct phases, specifically nickel-iron nanoparticles embedded in the K_2BDC matrix. XRD characterization of the post-reaction catalyst further confirms the existence of the K_2BDC phase. The fractured regions provide additional confirmation that the K_2BDC phase, which is sensitive to solution concentration and unstable, is a contributing factor to the structural instability of the reconstructed catalyst.

The reaction equations for the M_2-BDC-$(OH)_2$ precatalyst when subjected to varying concentrations of alkaline solutions are shown as follows

$$M_2 - BDC - (OH)_2 + 2KOH_{\mathrm{highconc.}} \rightarrow 2M(OH)_2\,(s) + K_2BDC\,(s) \quad (1)$$

$$M_2 - BDC - (OH)_2 + 2KOH_{\mathrm{lowconc.}} \rightarrow 2M(OH)_2\,(s) + 2K^+ + BDC^{2-} \quad (2)$$

M_2-BDC-$(OH)_2$ contains 2D metal layers that are separated by BDC ligand interlayers viewed from the *b*-axis. When the M_2-BDC-$(OH)_2$ precatalyst is employed for alkaline OER catalysis, the BDC ligands undergo leaching into the solution, resulting in the in situ reprecipitation of leached metal ions (M^{2+}), concomitant with the electro-oxidation of M^{2+} species to $M^{3+}OOH$ species. The leaching of ligands induces the emergence of pores in the reconstructed catalysts. These pores facilitate the profound infiltration of the solution and the subsequent leaching of internal ligands, which trigger a chain reconstruction reaction until it ends. The swift leaching of substantial ligands and the simultaneous in situ dissolution–reprecipitation of metal ions result in the formation of a low-crystalline structure with numerous pores and topology-guided morphologies. Therefore, the reconstructed catalyst generally possesses an integrated structure with high porosity and low crystallinity.

Based on the above analysis, the detachment mechanism of M_2-BDC-$(OH)_2$ precatalyst is illustrated (Figure 3d). Upon direct testing of the M_2-BDC-$(OH)_2$ precatalyst in a high-concentration alkali environment, the high concentration of hydroxide ions facilitates an etching reaction, resulting in the substantial leaching out of ligands. Given the high concentration of K^+ and the limited solubility of K_2BDC, the reaction generates numerous insoluble K_2BDC and in situ forms a $M(OH)_2$-K_2BDC phase separation structure. Density functional theory simulations reveal an increase of 37.3% in the cell volume of the derivative following the etching reaction of Ni_2-BDC-$(OH)_2$, with the formed K_2BDC occupying up to 71.8% of the volume across the two phases. Notably, K_2BDC exhibits inherent instability in aqueous

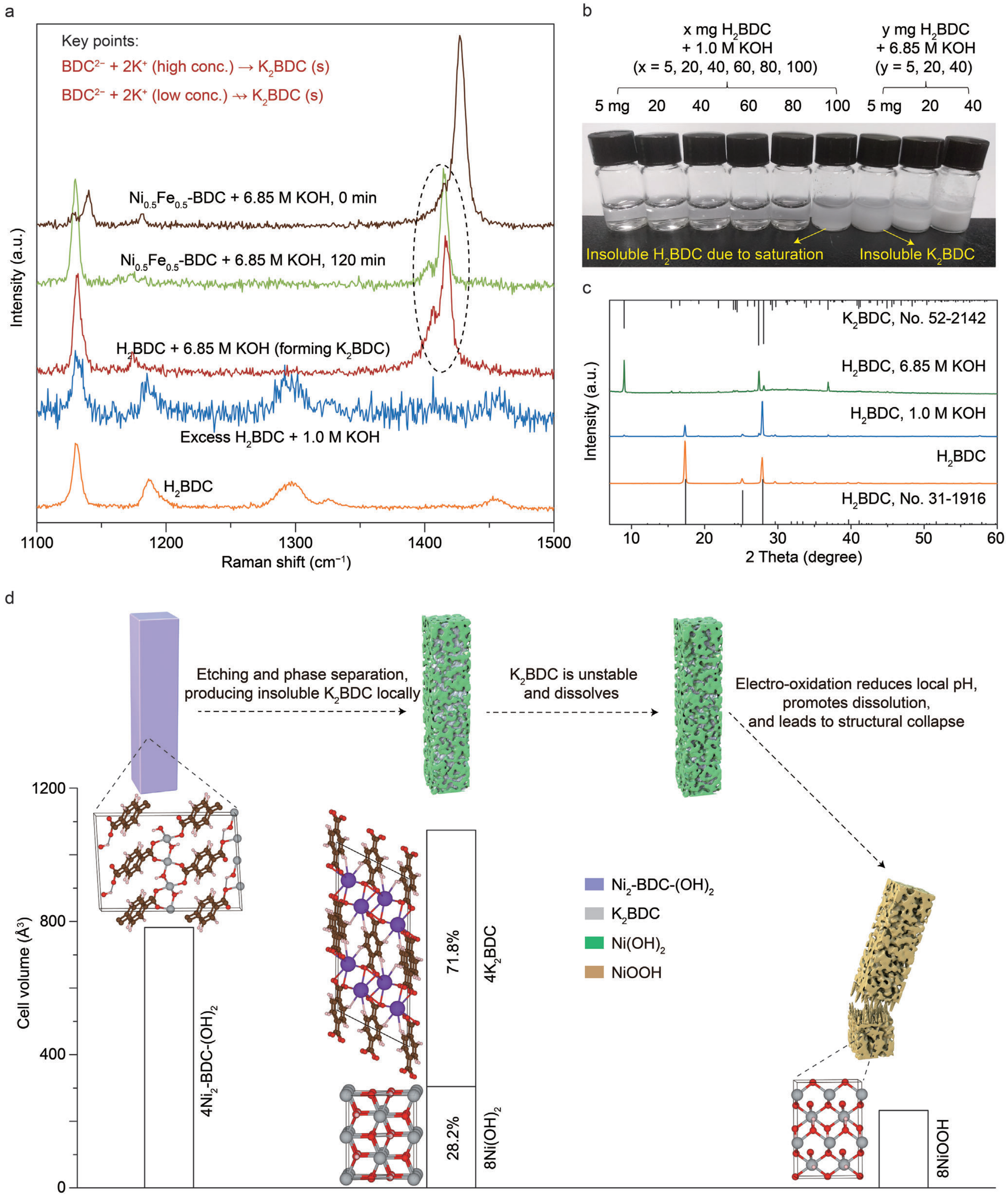

Figure 3. a) Raman spectra of H_2BDC powder, excess H_2BDC-1 м KOH mixture, H_2BDC-6.85 м KOH mixture, $Ni_{0.5}Fe_{0.5}$-BDC/NF samples before and after immersion in 6.85 м KOH for 120 min, confirming that a high-concentration alkali enables the formation of K_2BDC. b) Optical photo of different amounts of H_2BDC powders fully dispersed in 1 mL of 1 м KOH or 6.85 м KOH. c) XRD patterns of H_2BDC powder, excess H_2BDC-1 м KOH mixture, and H_2BDC-6.85 м KOH mixture. d) Calculated cell volume of the involved crystal structure during reconstruction processes, showing that the generation of unstable K_2BDC is accountable for the catalyst detachment.

solutions and manifests sensitivity to solution concentration. Particularly pronounced during the electro-oxidation process with gas spillover, changes in the local reaction environment exacerbate the instability of K_2BDC, resulting in structural collapse and the subsequent detachment of the catalyst. Consequently, following direct testing in 6.85 м KOH, the black suspended precipitations are observed and the solution becomes cloudy (FigureS9a, Supporting Information).

When the M_2-BDC-$(OH)_2$ precatalyst is tested in a low-concentration alkali, the slow alkali etching reaction prevents the rapid and large production of leached BDC ligands. Owing to the high solubility of K_2BDC in a low-concentration alkali, the electrochemical reconstruction process does not yield solid K_2BDC. Consequently, the ligands smoothly dissolve into the solution, avoiding any detrimental impact on the structural integrity of the reconstructed catalyst. The solution maintains transparency following testing in 1 м KOH (Figure S9b, Supporting Information). Therefore, the M_2-BDC-$(OH)_2$ precatalyst demonstrates different mechanical stabilities in different alkali concentrations, which depends on whether an insoluble K_2BDC solid is generated.

2.3. The Critical Point and Influencing Factors of Detachment

In order to find the critical alkali concentration for catalyst detachment, the intrinsic relationships between the dissolution characteristics of K_2BDC and the alkali concentration are studied. Initially, an efficient method for K_2BDC preparation is determined through an exploration of the acid-base reaction between H_2BDC and KOH. As shown in **Figure** 4a, in a low-concentration KOH solution, the addition of a small amount of H_2BDC results in the absence of any solid formation (yellow area). Conversely, the introduction of excess H_2BDC leads to undissolved H_2BDC (green area), which is attributed to the complete consumption of OH^- and the insolubility of H_2BDC in a neutral aqueous solution. In contrast, in a high-concentration KOH solution, a solid precipitate of K_2BDC is formed even with a very small amount of H_2BDC added (blue area). Therefore, K_2BDC powder can be prepared by adding H_2BDC to a high-concentration KOH solution.

Then, 0.032 mmol of K_2BDC is introduced into various concentrations of KOH solutions, guided by the quantity of K_2BDC produced during the complete reconstruction of $Ni_{0.5}Fe_{0.5}$-BDC. As shown in Figure 4b, the complete dissolution of K_2BDC is impeded when the KOH concentration exceeds 5 м. This critical point is in good agreement with the results of electron microscopy, wherein the absence of detachment phenomena is observed in 4.6 м KOH, contrasting with its occurrence in 5.2 м. Moreover, there is a deterioration in the detachment phenomenon with increasing concentration. Consequently, for the KOH solution system, the pivotal concentration for critical detachment in the phase reconstruction of $Ni_{0.5}Fe_{0.5}$-BDC precatalyst is identified as 5 м.

Other affecting factors have also been considered (Figure 4c). First, the types of reaction: OER, UOR, and HER. These reactions correspond to different applied biases. Under different states, the catalyst peels off from the conductive foam substrate in industrial high-concentration alkali, contrasted with its commendable mechanical stability at low concentrations (Figure S6, Supporting Information). Second, the types of alkaline solutions: AOH solutions, where A represents Li, Na, or K. The situation in NaOH solution is similar to that in KOH, and high concentrations of NaOH also induce catalyst detachment, whereas favorable mechanical stability is retained at low NaOH concentrations (Figure S10, Supporting Information). Third, the operating temperatures: considering the typical operating temperature range of industrial alkaline water electrolysis systems, which is usually between 50 and 90 °C. It is observed that high temperatures accelerate ligand leaching and the rapid production of K_2BDC, leading to the structural collapse of the catalyst (Figure S11, Supporting Information). Finally, the metal types in M_2-BDC-$(OH)_2$, where M represents Co, Ni, Cu, or Zn, etc. The detachment phenomenon based on different metals still exists in 6.85 м KOH, indicating that detachment is a common issue.

Furthermore, terephthalic acid coordinated metal-based catalysts, considered a typical catalytic material, have been extensively explored in catalytic applications (Figure S12, Supporting Information)[23–29] such as $NiRu_{0.13}$-BDC[29] and M@Ni-BDC (M = Ru, Ir, Pd)[30] for hydrogen evolution, and Ni-M-BDC (M = Fe, Co, Cu, Mn, or Zn)[25] and Ni-Fe-BDC[26] for oxygen evolution. When applied for catalysis in alkali environments, existing literature predominantly attributes high catalytic performances to the pristine BDC-based materials, and the theoretical analysis models commonly rely on the BDC-based structure. While the chemical or electrochemical stabilities of BDC-based materials and their evolution have not received much attention, particularly under realistic industrial conditions. This study contributes valuable insights by confirming the inherent instability of BDC-based materials in alkali environments, and thus they can only serve as precatalysts. Different from the reported results based on non-industrial parameters, the present work reveals anomalous detachment phenomena of M-BDC precatalysts under industrial conditions, and highlights the necessity for a comprehensive understanding of the stability and evolution of catalysts, especially when employed in practical applications.

2.4. Directional Reconstruction Regulation for Solving the Detachment Issue

In addressing the identified scientific issue, our proposed solution involves the implementation of a directional reconstruction regulation through a gradient test strategy (**Figure** 5a,b). This directional regulation changes the reconstruction behavior without generating adverse phase separation products. Notably, when subjected to a sequential testing procedure, commencing with tests in KOH solutions below 5 м or low-concentration NaOH/LiOH, followed by subsequent testing in industrial high-concentration KOH (referred to as the gradient test method), no discernible detachment phenomenon is observed. For instance, in a representative first-step test conducted in 1 м KOH, the obtained R_1-BDC/nickel foam maintains its original appearance when tested in 6.85 м KOH. Impressively, its durability reached 1000 h, with an activity decay rate of 0.0418 mV h^{-1} at 0.01 A cm^{-2}, and 300 h with an activity decay rate of 0.0305 mV h^{-1} at 0.2 A cm^{-2} (Figure S13, Supporting Information). Its stability life reaches the standards for commercial alkaline water electrolysis

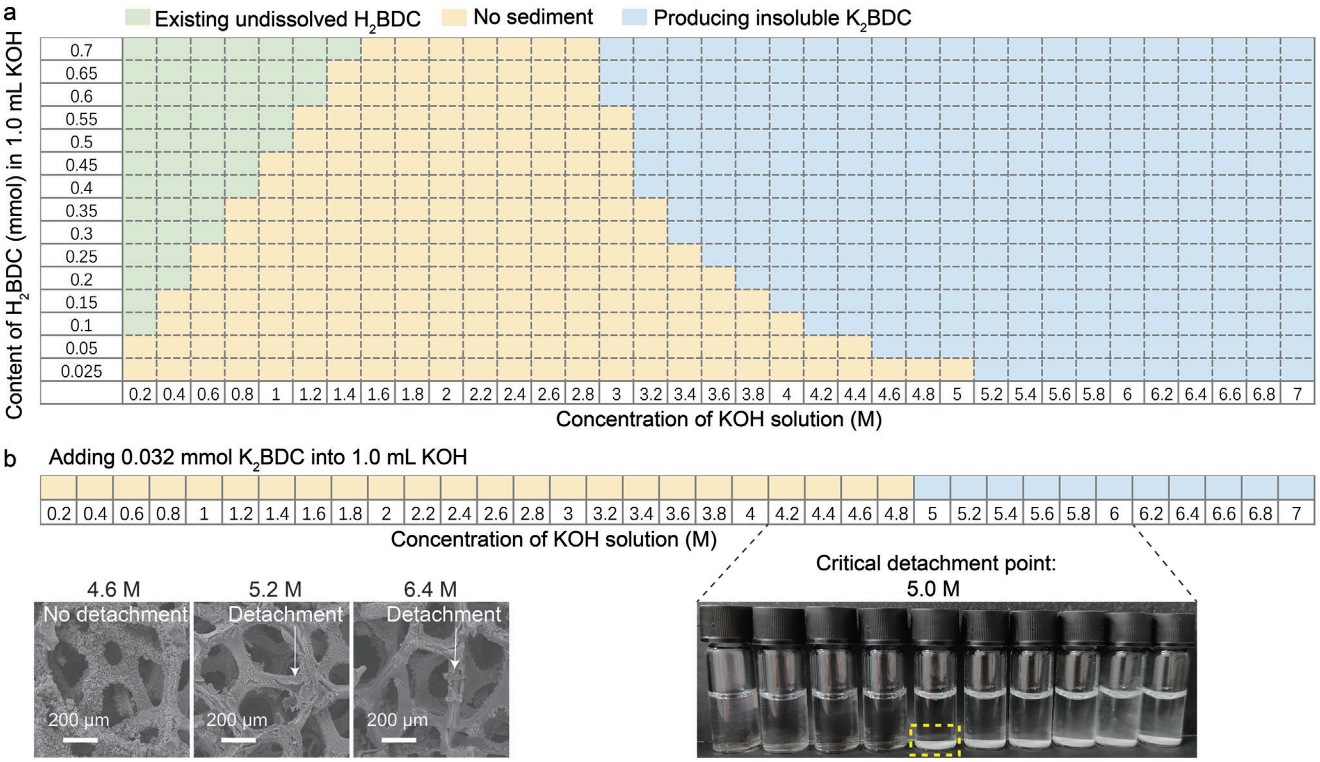

a

🟩 Existing undissolved H_2BDC 🟨 No sediment 🟦 Producing insoluble K_2BDC

Content of H_2BDC (mmol) in 1.0 mL KOH	0.2	0.4	0.6	0.8	1	1.2	1.4	1.6	1.8	2	2.2	2.4	2.6	2.8	3	3.2	3.4	3.6	3.8	4	4.2	4.4	4.6	4.8	5	5.2	5.4	5.6	5.8	6	6.2	6.4	6.6	6.8	7
0.7	🟩	🟩	🟩	🟩	🟩	🟩	🟩	🟨	🟨	🟨	🟨	🟨	🟨	🟨	🟦	🟦	🟦	🟦	🟦	🟦	🟦	🟦	🟦	🟦	🟦	🟦	🟦	🟦	🟦	🟦	🟦	🟦	🟦	🟦	🟦
0.65	🟩	🟩	🟩	🟩	🟩	🟩	🟨	🟨	🟨	🟨	🟨	🟨	🟨	🟨	🟦	🟦	🟦	🟦	🟦	🟦	🟦	🟦	🟦	🟦	🟦	🟦	🟦	🟦	🟦	🟦	🟦	🟦	🟦	🟦	🟦
0.6	🟩	🟩	🟩	🟩	🟩	🟩	🟨	🟨	🟨	🟨	🟨	🟨	🟨	🟨	🟦	🟦	🟦	🟦	🟦	🟦	🟦	🟦	🟦	🟦	🟦	🟦	🟦	🟦	🟦	🟦	🟦	🟦	🟦	🟦	🟦
0.55	🟩	🟩	🟩	🟩	🟩	🟨	🟨	🟨	🟨	🟨	🟨	🟨	🟨	🟨	🟨	🟦	🟦	🟦	🟦	🟦	🟦	🟦	🟦	🟦	🟦	🟦	🟦	🟦	🟦	🟦	🟦	🟦	🟦	🟦	🟦
0.5	🟩	🟩	🟩	🟩	🟩	🟨	🟨	🟨	🟨	🟨	🟨	🟨	🟨	🟨	🟨	🟦	🟦	🟦	🟦	🟦	🟦	🟦	🟦	🟦	🟦	🟦	🟦	🟦	🟦	🟦	🟦	🟦	🟦	🟦	🟦
0.45	🟩	🟩	🟩	🟩	🟨	🟨	🟨	🟨	🟨	🟨	🟨	🟨	🟨	🟨	🟨	🟦	🟦	🟦	🟦	🟦	🟦	🟦	🟦	🟦	🟦	🟦	🟦	🟦	🟦	🟦	🟦	🟦	🟦	🟦	🟦
0.4	🟩	🟩	🟩	🟩	🟨	🟨	🟨	🟨	🟨	🟨	🟨	🟨	🟨	🟨	🟨	🟦	🟦	🟦	🟦	🟦	🟦	🟦	🟦	🟦	🟦	🟦	🟦	🟦	🟦	🟦	🟦	🟦	🟦	🟦	🟦
0.35	🟩	🟩	🟩	🟨	🟨	🟨	🟨	🟨	🟨	🟨	🟨	🟨	🟨	🟨	🟨	🟨	🟦	🟦	🟦	🟦	🟦	🟦	🟦	🟦	🟦	🟦	🟦	🟦	🟦	🟦	🟦	🟦	🟦	🟦	🟦
0.3	🟩	🟩	🟩	🟨	🟨	🟨	🟨	🟨	🟨	🟨	🟨	🟨	🟨	🟨	🟨	🟨	🟦	🟦	🟦	🟦	🟦	🟦	🟦	🟦	🟦	🟦	🟦	🟦	🟦	🟦	🟦	🟦	🟦	🟦	🟦
0.25	🟩	🟩	🟨	🟨	🟨	🟨	🟨	🟨	🟨	🟨	🟨	🟨	🟨	🟨	🟨	🟨	🟨	🟦	🟦	🟦	🟦	🟦	🟦	🟦	🟦	🟦	🟦	🟦	🟦	🟦	🟦	🟦	🟦	🟦	🟦
0.2	🟩	🟩	🟨	🟨	🟨	🟨	🟨	🟨	🟨	🟨	🟨	🟨	🟨	🟨	🟨	🟨	🟨	🟨	🟦	🟦	🟦	🟦	🟦	🟦	🟦	🟦	🟦	🟦	🟦	🟦	🟦	🟦	🟦	🟦	🟦
0.15	🟩	🟨	🟨	🟨	🟨	🟨	🟨	🟨	🟨	🟨	🟨	🟨	🟨	🟨	🟨	🟨	🟨	🟨	🟨	🟦	🟦	🟦	🟦	🟦	🟦	🟦	🟦	🟦	🟦	🟦	🟦	🟦	🟦	🟦	🟦
0.1	🟩	🟨	🟨	🟨	🟨	🟨	🟨	🟨	🟨	🟨	🟨	🟨	🟨	🟨	🟨	🟨	🟨	🟨	🟨	🟨	🟦	🟦	🟦	🟦	🟦	🟦	🟦	🟦	🟦	🟦	🟦	🟦	🟦	🟦	🟦
0.05	🟨	🟨	🟨	🟨	🟨	🟨	🟨	🟨	🟨	🟨	🟨	🟨	🟨	🟨	🟨	🟨	🟨	🟨	🟨	🟨	🟨	🟨	🟦	🟦	🟦	🟦	🟦	🟦	🟦	🟦	🟦	🟦	🟦	🟦	🟦
0.025	🟨	🟨	🟨	🟨	🟨	🟨	🟨	🟨	🟨	🟨	🟨	🟨	🟨	🟨	🟨	🟨	🟨	🟨	🟨	🟨	🟨	🟨	🟨	🟨	🟨	🟦	🟦	🟦	🟦	🟦	🟦	🟦	🟦	🟦	🟦

Concentration of KOH solution (M)

b

Adding 0.032 mmol K_2BDC into 1.0 mL KOH

0.2	0.4	0.6	0.8	1	1.2	1.4	1.6	1.8	2	2.2	2.4	2.6	2.8	3	3.2	3.4	3.6	3.8	4	4.2	4.4	4.6	4.8	5	5.2	5.4	5.6	5.8	6	6.2	6.4	6.6	6.8	7
🟨	🟨	🟨	🟨	🟨	🟨	🟨	🟨	🟨	🟨	🟨	🟨	🟨	🟨	🟨	🟨	🟨	🟨	🟨	🟨	🟨	🟨	🟨	🟨	🟦	🟦	🟦	🟦	🟦	🟦	🟦	🟦	🟦	🟦	🟦

Concentration of KOH solution (M)

c

$Ni_{0.5}Fe_{0.5}$-BDC (Ni&Fe salts + BDC ligands) soaking in 6.85 M KOH at room temperature														
	For different reaction types			In different solutions			At different temperatures (°C)				Using different metal salts			
	OER	UOR	HER	High conc. NaOH	Low conc. NaOH	Sat. LiOH	20	40	60	80	Co	Ni	Cu	Zn
Whether detachment during reaction	√	√	√	--			--				--			
Whether detachment during soaking	--			√	×	×	√	√	√	√	√	√	√	√
Whether detachment during OER	--			√	×	×	√	√	√	√	√	√	√	√

Figure 4. a) Correlation among terephthalic acid content, the concentration of alkali solution, and product properties, indicating that K_2BDC can only be produced in a high-concentration alkali. b) Solubility of K_2BDC powder with a certain number of moles in different concentrations of alkali, and 5 M is a critical concentration. SEM images represent the microscopic morphologies of $Ni_{0.5}Fe_{0.5}$-BDC/NF after OER in different concentrations of alkali. The detachment phenomenon begins to occur when the concentration reaches 5.2 M. c) Effects of reaction types, electrolytes, test temperatures, and metal compositions in the complex on the detachment behavior.

application,[31] and its minimal potential fluctuation confirms excellent catalytic stability under industrial conditions. After testing, no detachment catalyst is observed (Figure S9c, Supporting Information).

The electrochemical behavior of $Ni_{0.5}Fe_{0.5}$-BDC/NF in varying concentrations of alkali is systematically compared (Figure S14, Supporting Information). Both curves exhibit an activation range with decreasing overpotential values at the beginning and followed by a tendency to stabilize. When tested in 1 M KOH, it takes ≈1 h for the potential to gradually decrease to a stable stage, which is attributed to the production of an increased quantity of reconstructed active species. In contrast, when tested in 6.85 M KOH, the potential experiences a rapid decline within 100 s and then increases slowly to a stable stage. This ascending stage is ascribed to the ongoing detachment of the catalyst during the reconstruction and stabilization processes.

The oxygen evolution performances between the direct test (R_2-BDC catalyst) and the gradient test (R_1-BDC catalyst) are further compared under industrial conditions of 6.85 M KOH and 80 °C (Figure 5c). The R_1-BDC catalyst requires a lower applied potential at various current densities, such as a potential difference of ≈60 mV at 2 A cm^{-2}. The R_1-BDC catalyst shows

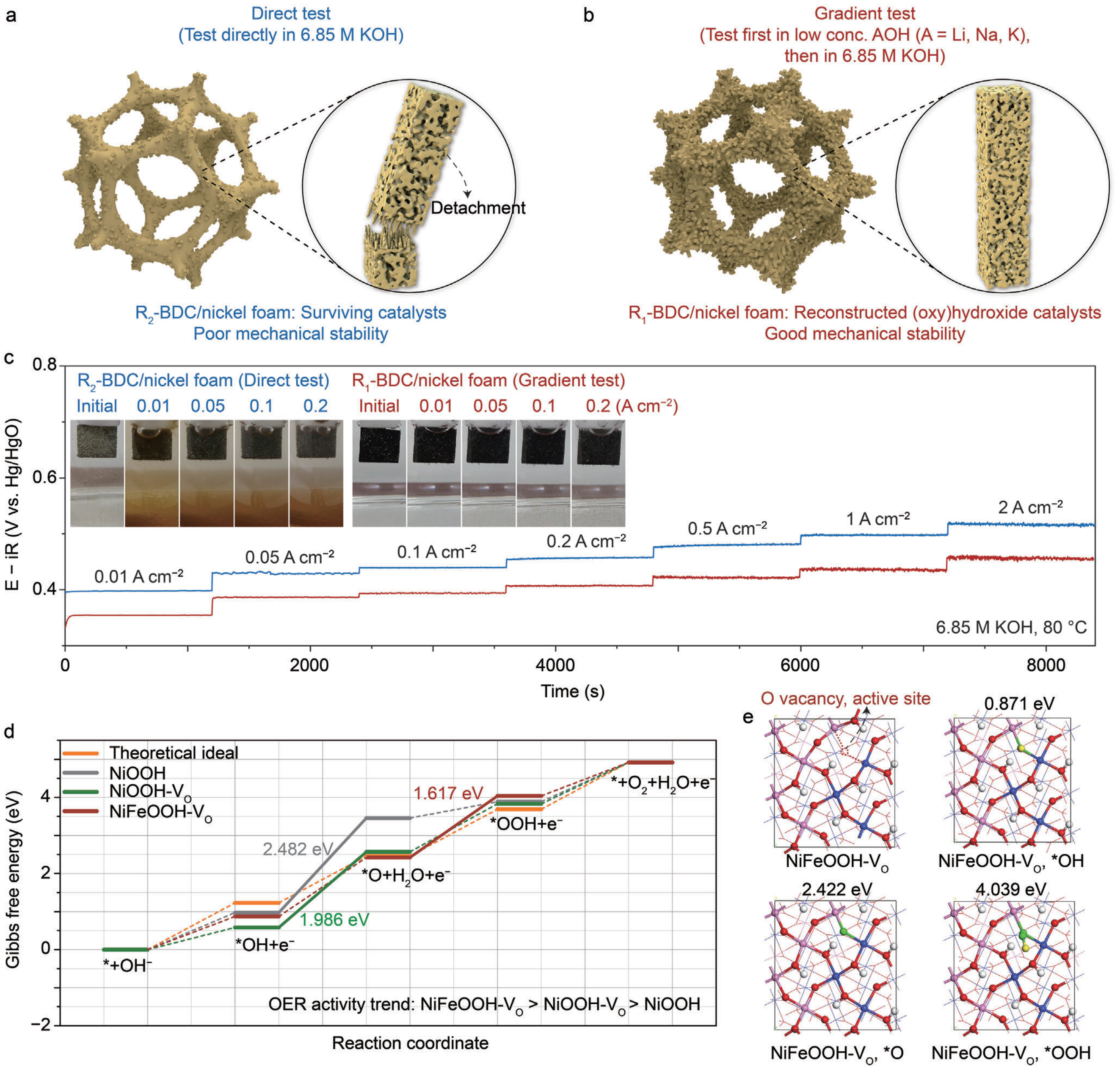

Figure 5. a,b) Comparison of the structural configuration diagrams for reconstructed catalysts (R_2-BDC and R_1-BDC, respectively) obtained by traditional direct test methods (a) and gradient test methods (b) proposed by this work. The former obtains a surviving catalyst with poor mechanical stabilities and the latter results in catalysts with excellent mechanical stabilities. c) Chronopotentiometric curves of R_2-BDC/nickel foam and R_1-BDC/nickel foam at different current densities in 6.85 M KOH at 80 °C. Insets are representative optical photos during chronopotentiometric tests at different current densities. d) Gibbs free energy of each reaction step on different models, considering the effects of iron incorporation and O vacancy on OER activity. e) DFT-calculated models (white-H, red-O, blue-Ni, and pink-Fe) with the optimal structures for pristine NiFeOOH-V_O (with 25% Fe doping) and intermediate products. The ball-and-stick model is highlighted by the first layer of atoms on the surface, and the atoms in 2–4 layers are represented by lines.

excellent mechanical stability at different current densities, however, the R_2-BDC catalyst peels off seriously (Insets in Figure 5c). Moreover, the comparative analysis elucidates a high structural similarity between R_1-BDC and R_2-BDC catalysts, exhibiting features such as complete reconstruction, low crystallinity, and high porosity (Figure S15, Supporting Information). Therefore, the primary difference in performance lies in the quantity of loaded reconstructed species. The gradient test strategy, by effectively averting the detachment of the reconstructed catalyst, manifests a higher abundance of reconstructed species, thereby exhibiting superior catalytic performance.

The high intrinsic OER activity of the R_1-BDC catalyst is further revealed. It possesses abundant oxygen vacancies through the O 1s in X-ray photoelectron spectroscopy (XPS)

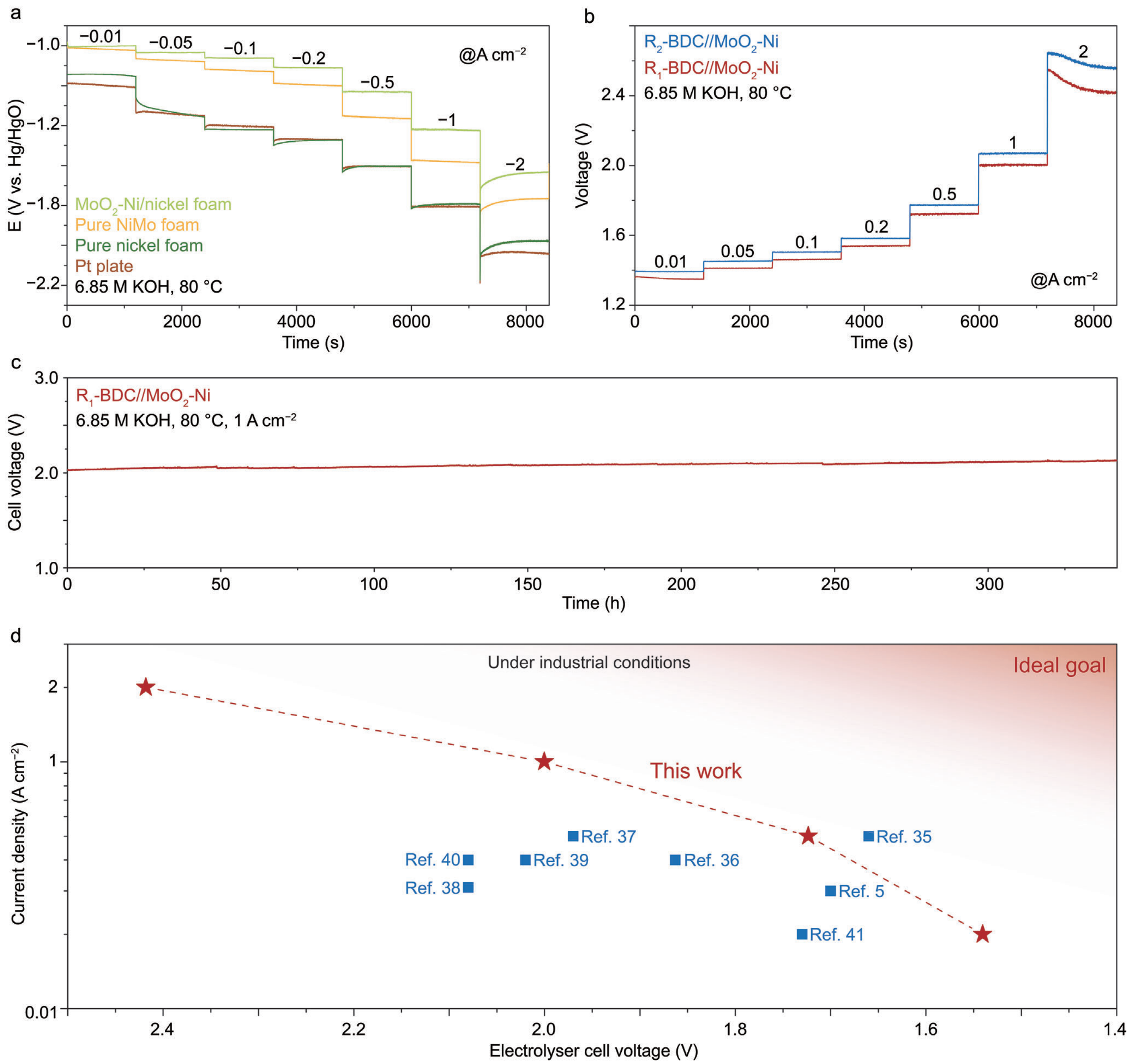

Figure 6. a) Chronopotentiometric curves of the Pt plate, pure nickel foam, pure NiMo foam, and MoO_2-Ni/nickel foam at different current densities in 6.85 м KOH at 80 °C. b) Cell voltage–time curves of R_1-BDC//MoO_2-Ni and R_2-BDC//MoO_2-Ni based electrolyzers held at different current densities in 6.85 м KOH at 80 °C. c) Cell voltage–time curves of R_1-BDC//MoO_2-Ni based electrolyzer held at 1 A cm^{-2} in 6.85 м KOH at 80 °C. d) Alkaline water electrolysis performance comparison of representative OER//HER paired catalysts under industrial conditions in this work and reported results.

analysis (Figure S15e, Supporting Information). Based on the inductively coupled plasma atomic emission spectrometry (ICP-AES) results, the Fe/(Fe+Ni) atomic ratio of the R_1-BDC catalyst is 0.293. Therefore, the chemical formula of R_1-BDC is expressed as $Fe_{0.3}Ni_{0.7}OOH$. This value is slightly smaller than that observed in precatalyst (0.372), indicating the leaching of iron species during electrochemical testing, which is common in nickel-iron-based oxygen evolution catalysts.[32,33] Further elemental mappings demonstrate the uniform distributions of Ni, Fe, and O elements (Figure S15f, Supporting Information), suggesting that there are no separate phases after reconstruction.

To elucidate the crucial roles of iron and oxygen vacancies in reconstructed R_1-BDC catalyst, we employ three density function theory (DFT) models for comprehensive calculations and analyses including ideal NiOOH surface, NiOOH-V_O, and NiFeOOH-V_O models (Figure S16, Supporting Information). The calculated results in Figure 5d confirm a clear trend of OER activity: NiFeOOH-V_O > NiOOH-V_O > NiOOH. The poor activity of the pristine NiOOH is mainly due to the formation of O* step (step 2) with too weak adsorption of O*, and its largest Gibbs free energy difference (ΔG_{max}) value is 2.482 eV. When the oxygen vacancy is constructed to expose the double Ni atomic active site (i.e., NiOOH-V_O model), the catalytic activity can be improved, while the adsorption of OH* is still too strong with ΔG_{max} of 1.986 eV. In the NiFeOOH-V_O model, iron doping can reduce the adsorption of OH*, thereby modulating the ΔG at each step to a state closer to the ideal 1.23 eV. The rate-determining step (RDS) changes from the formation of O* step (step 2) in NiOOH and NiOOH-V_O species into the formation of OOH* step (step 3) in NiFeOOH-V_O, with the lowest ΔG_{max} value of 1.617 eV. As shown in Figure 5e, the O vacancy adjacent to nickel and iron atoms serves as the active site, establishing the co-effect of iron doping and oxygen vacancy as pivotal contributors to significantly increase the intrinsic OER activity of NiOOH.

In addition, in nickel (oxy)hydroxide OER catalysts, controlling iron incorporation amounts causes different catalytic activities.[22,34] As shown in Figure S17, Supporting Information, the catalytic activity as a function of iron content is presented in a volcanic structure for $Ni_{1-x}Fe_x$-BDC/NF catalysts. When the x value is between 0.3 and 0.6, the obtained reconstructed catalysts are at the top of the volcanic structure and exhibit excellent catalytic activity. Therefore, the $Ni_{0.5}Fe_{0.5}$-BDC/NF is identified as an optimal precatalyst for subsequent performance evaluations in alkaline water electrolysis devices. The reconstructed $Ni_{1-x}Fe_x$-BDC catalysts are fully retained on the foam (Figure S18, Supporting Information), proving the success of the gradient test strategy in solving the detachment issue.

To pair with R_1-BDC/nickel foam and evaluate their alkaline water electrolysis performances, the HER performance of MoO_2-Ni nanowire arrays grown on nickel foam (MoO_2-Ni/nickel foam, Figure S19, Supporting Information) was evaluated in 6.85 м KOH at 80 °C. As shown in **Figure 6**a, the MoO_2-Ni/nickel foam catalyst exhibits the highest catalytic activities when compared with commercial NiMo foam, commercial nickel foam, and Pt plate. During testing, the graphite rod electrode at the oxygen evolution ends peels off under harsh conditions due to electrochemical oxidation and a large amount of produced gas. Subsequently, the alkaline water electrolysis performances of R_1-BDC//MoO_2-Ni and R_2-BDC//MoO_2-Ni paired catalysts were evaluated using a small alkaline electrolyzer cell (Figure 6b and Figure S20, Supporting Information). The coupled R_1-BDC//MoO_2-Ni system exhibits a lower cell voltage to achieve current densities of 0.01, 0.05, 0.1, 0.2, 0.5, 1, and 2 A cm^{-2}, and the required cell voltage values are 1.349, 1.413, 1.463, 1.540, 1.723, 2.000, and 2.418 V, respectively. No appreciable increase in the cell voltage during 340 h (over 14 days) of continuous operation at 1 A cm^{-2} is observed (Figure 6c). These results are superior to several sets of reported results under industrial conditions[5,35–41] (Figure 6d and Table S1, Supporting Information).

3. Conclusion

In this study, we elucidate and clarify the distinct reconstruction chemistries of terephthalic acid-coordinated oxygen-evolving precatalysts between laboratory test conditions and industrial operating conditions. Unlike what is observed in the laboratory low-concentration alkali (0.1–1 м KOH), a severe detachment issue arises with the reconstructed (oxy)hydroxide catalyst when directly applied in industrial high-concentration conditions (exceeding 5 м KOH). This observed phenomenon is attributed to the formation of the K_2BDC separate phase, induced by substantial ligand leaching in the presence of high-concentration alkali. Consequently, the accumulation of solid K_2BDC and its instability leads to catalyst breakage and detachment.

The elucidation of the detachment mechanism, identification of critical points, and the correlation between operating parameters and detachment are clearly presented through systematically studying the effects of catalytic reaction types, solution types and concentrations, operating temperatures, and precatalyst types. Subsequently, a novel gradient test strategy is proposed for achieving targeted reconstruction and smooth ligand leaching, effectively solving the detachment issue. Importantly, this method exhibits broad applicability across a series of precatalysts for diverse catalytic reactions. Under industrial operating conditions, the reconstructed catalysts demonstrate excellent OER activity, attributed to the co-effect of iron doping and oxygen vacancy. The designed electrolyzer, employing directionally reconstructed catalysts, only requires 2 V of cell voltage to achieve an industrially relevant current density of 1 A cm^{-2} in 6.85 м KOH at 80 °C, with negligible attenuation observed over 340 h. This work bridges the gap between the promising reconstructed catalysts studied under laboratory test conditions and their practical viability in industrial settings, thereby facilitating the development of catalysts under realistic conditions.

Supporting Information

Supporting Information is available from the Wiley Online Library or from the author.

Acknowledgements

This work was supported by the National Key Research and Development Program of China (2022YFB3803401, 2023YFB3809304), the National Natural Science Foundation of China (22209151, 52302318, 52273234), the China Postdoctoral Science Foundation (2022TQ0280, 2022M722856), Henan Province Science and Technology Research and Development Plan Joint Fund (232301420031), National Key Research and Development Program of Henan Province (231111240200), and the National Natural Science Fund for Excellent Young Scientists Fund Program (Overseas). The Supercomputing Center of USTC and Hefei Advanced Computing Center were acknowledged.

Conflict of Interest

The authors declare no conflict of interest.

Data Availability Statement

The data that support the findings of this study are available from the corresponding author upon reasonable request.

Keywords

directionally reconstructed catalyst, dual site regulation, laboratory versus industrial conditions, real-time monitoring, reconstruction and detachment behavior

Received: December 20, 2023
Revised: March 20, 2024

[1] X. Liu, J. S. Meng, J. X. Zhu, M. Huang, B. Wen, R. T. Guo, L. Q. Mai, *Adv. Mater.* **2021**, *33*, 2007344.
[2] H. Ding, H. F. Liu, W. S. Chu, C. Z. Wu, Y. Xie, *Chem. Rev.* **2021**, *121*, 13174.
[3] L. K. Gao, X. Cui, C. D. Sewell, J. Li, Z. Q. Lin, *Chem. Soc. Rev.* **2021**, *50*, 8428.
[4] J. Wang, S.-J. Kim, J. P. Liu, Y. Gao, S. Choi, J. Han, H. Shin, S. Jo, J. Kim, F. Ciucci, H. Kim, Q. T. Li, W. L. Yang, X. Long, S. H. Yang, S.-P. Cho, K. H. Chae, M. G. Kim, H. Kim, J. Lim, *Nat. Catal.* **2021**, *4*, 212.
[5] B. Zhang, L. Wang, Z. Cao, S. M. Kozlov, F. P. García de Arquer, C. T. Dinh, J. Li, Z. Y. Wang, X. L. Zheng, L. S. Zhang, Y. Z. Wen, O. Voznyy, R. Comin, P. D. Luna, T. Regier, W. L. Bi, E. E. Alp, C.-W. Pao, L. R. Zheng, Y. F. Hu, Y. Y. Ji, Y. Y. Li, Y. Zhang, L. Cavallo, H. S. Peng, E. H. Sargent, *Nat. Catal.* **2020**, *3*, 985.
[6] X. Liu, K. Ni, B. Wen, R. T. Guo, C. J. Niu, J. S. Meng, Q. Li, P. J. Wu, Y. W. Zhu, X. J. Wu, L. Q. Mai, *ACS Energy Lett.* **2019**, *4*, 2585.
[7] X. Liu, J. S. Meng, K. Ni, R. T. Guo, F. J. Xia, J. J. Xie, X. Li, B. Wen, P. J. Wu, M. Li, J. S. Wu, X. J. Wu, L. Q. Mai, D. Y. Zhao, *Cell Rep. Phys. Sci.* **2020**, *1*, 100241.
[8] J. Villalobos, D. González-Flores, R. Urcuyo, M. L. Montero, G. Schuck, P. Beyer, M. Risch, *Adv. Energy Mater.* **2021**, *11*, 2101737.
[9] X. Liu, R. T. Guo, K. Ni, F. J. Xia, C. J. Niu, B. Wen, J. S. Meng, P. J. Wu, J. S. Wu, X. J. Wu, L. Q. Mai, *Adv. Mater.* **2020**, *32*, 2001136.
[10] M. Tang, W. T. Yuan, Y. Ou, G. X. Li, R. Y. You, S. D. Li, H. S. Yang, Z. Zhang, Y. Wang, *ACS Catal.* **2020**, *10*, 14419.
[11] L. An, Y. Hu, J. Y. Li, J. M. Zhu, M. Z. Sun, B. L. Huang, P. X. Xi, C.-H. Yan, *Adv. Mater.* **2022**, *34*, 2202874.
[12] Y. B. Chen, Y. M. Sun, M. Y. Wang, J. X. Wang, H. Y. Li, S. B. Xi, C. Wei, P. X. Xi, G. E. Sterbinsky, J. W. Freeland, A. C. Fisher, J. W. Ager, Z. X. Feng, Z. C. J. Xu, *Sci. Adv.* **2021**, *7*, eabk1788.
[13] J. T. Mefford, A. R. Akbashev, M. Kang, C. L. Bentley, W. E. Gent, H. T. D. Deng, D. H. Alsem, Y.-S. Yu, N. J. Salmon, D. A. Shapiro, P. R. Unwin, W. C. Chueh, *Nature* **2021**, *593*, 67.
[14] T.-H. Shen, L. Spillane, J. Y. Peng, Y. Shao-Horn, V. Tileli, *Nat. Catal.* **2022**, *5*, 30.
[15] S. L. Zhao, C. H. Tan, C.-T. He, P. F. An, F. Xie, S. Jiang, Y. F. Zhu, K.-H. Wu, B. W. Zhang, H. J. Li, J. Zhang, Y. Chen, S. Q. Liu, J. C. Dong, Z. Y. Tang, *Nat. Energy* **2020**, *5*, 881.
[16] T. Z. Wu, S. N. Sun, J. J. Song, S. B. Xi, Y. H. Du, B. Chen, W. A. Sasangka, H. B. Liao, C. L. Gan, G. G. Scherer, L. Zeng, H. J. Wang, H. Li, A. Grimaud, Z. C. J. Xu, *Nat. Catal.* **2019**, *2*, 763.
[17] A. Buttler, H. Spliethoff, *Renewable Sustainable Energy Rev.* **2018**, *82*, 2440.
[18] Z.-Y. Yu, Y. Duan, X.-Y. Feng, X. X. Yu, M.-R. Gao, S.-H. Yu, *Adv. Mater.* **2021**, *33*, 2007100.
[19] Y. T. Luo, L. Tang, U. Khan, Q. M. Yu, H.-M. Cheng, X. L. Zou, B. L. Liu, *Nat. Commun.* **2019**, *10*, 269.
[20] Y. T. Luo, Z. Y. Zhang, M. Chhowalla, B. L. Liu, *Adv. Mater.* **2021**, *34*, 2108133.
[21] Y. L. Chen, G. T. Yu, W. Chen, Y. P. Liu, G.-D. Li, P. W. Zhu, Q. Tao, Q. J. Li, J. W. Liu, X. P. Shen, H. Li, X. R. Huang, D. J. Wang, T. Asefa, X. X. Zou, *J. Am. Chem. Soc.* **2017**, *139*, 12370.
[22] M. W. Louie, A. T. Bell, *J. Am. Chem. Soc.* **2013**, *135*, 12329.
[23] Y. C. Hao, Q. L. Liu, Y. Zhou, Z. Q. Yuan, Y. N. Fan, Z. F. Ke, C.-Y. Su, G. Q. Li, *Energy Environ. Mater.* **2019**, *2*, 18.
[24] K. Rui, G. Q. Zhao, M. M. Lao, P. X. Cui, X. S. Zheng, X. B. Zheng, J. X. Zhu, W. Huang, S. X. Dou, W. P. Sun, *Nano Lett.* **2019**, *19*, 8447.
[25] J. Zhou, Z. K. Han, X. K. Wang, H. Y. Gai, Z. K. Chen, T. Guo, X. B. Hou, L. L. Xu, X. J. Hu, M. H. Huang, S. V. Levchenko, H. Q. Jiang, *Adv. Funct. Mater.* **2021**, *31*, 2102066.
[26] F.-L. Li, P. T. Wang, X. Q. Huang, D. J. Young, H.-F. Wang, P. Braunstein, J.-P. Lang, *Angew. Chem., Int. Ed.* **2019**, *58*, 7051.
[27] F.-X. Ma, F. C. Lyu, Y. X. Diao, B. B. Zhou, J. H. Wu, F. W. Kang, Z. B. Li, X. F. Xiao, P. Wang, J. Lu, Y. Y. Li, *Nano Res.* **2021**, *15*, 2887.
[28] W. J. Li, S. Watzele, H. A. El-Sayed, Y. C. Liang, G. Kieslich, A. S. Bandarenka, K. Rodewald, B. Rieger, R. A. Fischer, *J. Am. Chem. Soc.* **2019**, *141*, 5926.
[29] Y. M. Sun, Z. Q. Xue, Q. L. Liu, Y. L. Jia, Y. L. Li, K. Liu, Y. Y. Lin, M. Liu, G. Q. Li, C.-Y. Su, *Nat. Commun.* **2021**, *12*, 1369.
[30] L. M. Deng, F. Hu, M. Y. Ma, S.-C. Huang, Y. X. Xiong, H.-Y. Chen, L. L. Li, S. J. Peng, *Angew. Chem., Int. Ed.* **2021**, *60*, 22276.
[31] V. R. Stamenkovic, D. Strmcnik, P. P. Lopes, N. M. Markovic, *Nat. Mater.* **2016**, *16*, 57.
[32] D. Y. Chung, P. P. Lopes, P. F. B. D. Martins, H. Y. He, T. Kawaguchi, P. Zapol, H. You, D. Tripkovic, D. Strmcnik, Y. S. Zhu, S. Seifert, S. Lee, V. R. Stamenkovic, N. M. Markovic, *Nat. Energy* **2020**, *5*, 222.
[33] J. Liu, W. Du, S. Y. Guo, J. Pan, J. G. Hu, X. Y. Xu, *Adv. Sci.* **2023**, *10*, 2300717.
[34] D. Friebel, M. W. Louie, M. Bajdich, K. E. Sanwald, Y. Cai, A. M. Wise, M.-J. Cheng, D. Sokaras, T.-C. Weng, R. Alonso-Mori, R. C. Davis, J. R. Bargar, J. K. Norskov, A. Nilsson, A. T. Bell, *J. Am. Chem. Soc.* **2015**, *137*, 1305.
[35] C. Wang, P. L. Zhai, M. Y. Xia, Y. Z. Wu, B. Zhang, Z. W. Li, L. Ran, J. F. Gao, X. M. Zhang, Z. Z. Fan, L. C. Sun, J. G. Hou, *Angew. Chem., Int. Ed.* **2021**, *60*, 27126.
[36] B. Zhong, P. Y. Kuang, L. X. Wang, J. G. Yu, *Appl. Catal., B* **2021**, *299*, 120668.
[37] H. Wu, Z. C. Wang, Z. X. Li, Y. J. Ma, F. Ding, F. Q. Li, H. F. Bian, Q. X. Zhai, Y. L. Ren, Y. X. Shi, Y. R. Yang, Y. Deng, S. C. Tang, X. K. Meng, *Adv. Energy Mater.* **2023**, *13*, 2300837.
[38] H. Chen, J. H. Li, Y. C. Shen, W. Q. Jiao, J. P. Wang, Y. C. Zou, X. X. Zou, *Appl. Catal., B* **2022**, *316*, 121605.
[39] Q. L. Wen, K. Yang, D. J. Huang, G. Cheng, X. M. Ai, Y. W. Liu, J. K. Fang, H. Q. Li, L. Yu, T. Y. Zhai, *Adv. Energy Mater.* **2021**, *11*, 2102353.
[40] J.-T. Ren, L. Chen, H.-Y. Wang, W.-W. Tian, X.-L. Song, Q.-H. Kong, Z.-Y. Yuan, *ACS Catal.* **2023**, *13*, 9792.
[41] G. F. Qian, J. L. Chen, T. Q. Yu, J. C. Liu, L. Luo, S. B. Yin, *Nano-Micro Lett.* **2022**, *14*, 20.